ADVANCED FREE VORTEX WAKE METHOD FOR VARIABLE RPM ROTORS

Yuxi Chen, Hamed Haddad Khodaparast, and Alper Celik
Swansea University
Swansea, SA1 8EN, UK

Ye Yuan
University of Glasgow
Glasgow, G12 8QQ, UK

ABSTRACT

Free vortex wake (FVW) method is widely used for aerodynamic calculation of rotor systems, as it strikes a balance between accuracy and efficiency in rotorcraft flight dynamics and handling qualities analysis. However, limitations such as inaccuracy in the reverse flow region calculations in the FVW method prevents its application in variable RPM (VRPM) rotors. In this paper, the authors introduce several improvements to the current FVW method, including planar rigid near-wake reverse flow correction and improved far-wake generation method, enabling it for VRPM rotor simulations. The results obtained with the improved FVW method are compared against experimental data and show good agreement.

INTRODUCTION

Advanced air mobility (AAM) has drawn increased research attention in recent years, and most AAMs are utilising electric-powered multi-rotor configurations (Refs. 1–4). Thanks to modern electric motors having the capability of rapid acceleration and deceleration, AAMs are capable of using differential thrust control strategies, in which the thrust of each rotor on the vehicle is controlled independently by adjusting the rotational speed of the rotor. The variable RPM (VRPM) feature of AAMs enables simplified rotor hub design, greatly reducing the chance of mechanical failure. On the other hand, VRPM complicates the flight dynamics on multiple scales. In dynamics, varying the rotational speed of the rotor introduces additional torque to the vehicle due to the acceleration of the rotor mass. In aerodynamics, the wake structure created by VRPM rotors in forward flight would change dramatically when the rotational speed of the rotor changes, as the size of the reverse flow region is dependent on the rotor rotational speed. The alterations in dynamics and aerodynamics will be coupled, further complicating the flight dynamics of the vehicle.

Flight dynamics simulation modelling is one of the keystones for the development of AAMs, and there are currently many approaches to modelling the dynamics and aerodynamics of AAMs. High-fidelity methods such as computational fluid dynamics (CFD) provide detailed insight into rotor aerodynamics, but they are very computationally intensive (Refs. 5, 6). Low-fidelity methods, such as potential flow methods, prioritise computational efficiency and can achieve real-time simulation capabilities (Ref. 7). However, these simplified methods do not account for the aerodynamic interactions between blades and rotors. In the mid-fidelity range, various vortex-based methods manage to strike a balance between accuracy and efficiency. For example, ring-type vortex wake methods can efficiently simulate rotor-rotor aerodynamic interactions (Refs. 8, 9). However, they do not consider the aerodynamic interactions between blades, and do not accurately model the reverse flow region of the rotor during high-speed forward flight. The vortex lattice method (VLM) offers greater fidelity by having vortex generation from every blade element, albeit with a significant increase in computation cost (Ref. 10). Free vortex wake (FVW) method finds itself in between, simplifying the vortex generation to create only one vortex at the blade tip, which greatly reduces the computation cost compared with VLM, while having similar fidelity (Refs. 11, 12). Ongoing research on the linearisation of the FVW method is underway to achieve real-time simulation capability (Ref. 13). The FVW method has the capability to simulate aerodynamic interference between blades, and the rotor wake created by the blades can freely develop and interact with other wakes, rotor blades, and fuselages. However, the reverse flow region remains inaccurate, due to the planar rigid near-wake assumption and the neglect of the blade in-bound vortex. In addition, very limited research is currently being done on the aerodynamic interaction under VRPM conditions, despite the strong requirement for such modelling methods for flight analysis of AAMs.

In this article, the authors introduce several improvements to the current FVW model.

1. A reverse flow correction method that applies to the planar rigid near-wake assumption in the FVW method, aiming to fix the instability issue during iterations in the calculation of the blade bound vortex strength, which can greatly increase the accuracy of the reverse flow region as well as reducing iteration count.
2. An improved far-wake generation method that takes into consideration the potential influence of the far-wake generated, instead of being purely dependent on the maximum bound vortex strength.

Details of the improvements made to the FVW model are provided in the methodology section. Results obtained using the proposed improved method are presented through case studies, which include available experimental results for validation.

METHODOLOGY

The methodology section describes the improvements to the original FVW method introduced by Bagai (Ref. 11). These improvements are made to allow the FVW method to be used in VRPM conditions.

Planar rigid near-wake reverse flow correction

In the original FVW method, the near-wake is assumed to be planar and rigid relative to the blade, where the influence of the near-wake on the blade control point only needs to be calculated once prior to simulation. It has the advantage of reducing the computation cost while maintaining good accuracy in normal flight scenarios of the rotor, e.g. hover, low-speed forward flight. However, its accuracy deteriorates when the blade is in stall conditions or reverse flow conditions, e.g. high-speed forward flight. This limitation is not addressed in the original FVW method, as it assumed that the correlation between lift coefficient and attack angle to be linear. This assumption made the trim equation for bound vortex strength linear and solvable using a linear equation solver (Ref. 11). However, this assumption naturally neglected the effects of blade stall and reverse flow phenomena that become significant during high-speed forward flight and cannot be ignored. In our improved FVW method, a lookup table for lift and drag coefficients is utilised, making the bound vortex strength trim equation non-linear and requiring iterative solutions. This introduces a key issue with the planar rigid near-wake assumption. As shown in Fig. 1, in the reverse flow region of the blade, the inflow travels from the trailing edge to the leading edge, with angles of attack exceeding 90 degrees. Consequently, the near-wake is generated from the trailing edge

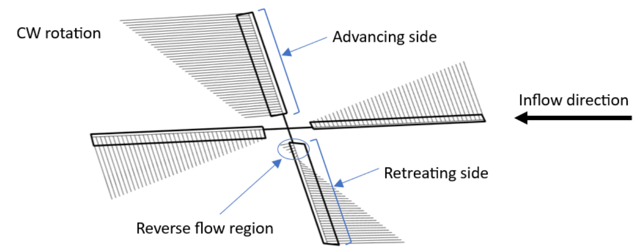

Figure 1. Near-wake distribution in forward flight

to the leading edge, reversing the induced velocity influence at the blade control point. Without any correction, the trim equation often requires more iterations and may converge to incorrect results in the reverse flow region, or in some cases, fail to converge at all. This instability compromises simulation accuracy, especially under VRPM conditions during high-speed forward flight, where the reverse flow region expands as the RPM decreases. To address this, a correction method has been developed to resolve the reverse flow issue associated with the planar rigid near-wake assumption. The method improves the accuracy of bound vortex strength calculation within the reverse flow region and enhances both computational efficiency and simulation stability when extensive reverse flow occurs. Figs. 2a and 2b show the bound vortex strength variation computed using the original and the improved near-wake model, respectively. As demonstrated, the improved near-wake model offers better stability and accuracy in the reverse flow region compared to the original approach.

Prior to the simulation, the vortex to blade control point induced velocity influence coefficient matrices for the bound vortex, $\boldsymbol{I}_{bound}$, and the trailed vortex, $\boldsymbol{I}_{trail}$, must be calculated using the Biot-Savart Law.

$$\boldsymbol{I}_{bound} = \begin{bmatrix} I_{b_{1,1}} & I_{b_{1,2}} & \cdots & I_{b_{1,j}} \\ I_{b_{2,1}} & I_{b_{2,2}} & \cdots & I_{b_{2,j}} \\ \vdots & \vdots & \ddots & \vdots \\ I_{b_{i,1}} & I_{b_{i,2}} & \cdots & I_{b_{i,j}} \end{bmatrix} \quad (1)$$

$$\boldsymbol{I}_{trail} = \begin{bmatrix} I_{t_{1,1}} & I_{t_{1,2}} & \cdots & I_{t_{1,j}} \\ I_{t_{2,1}} & I_{t_{2,2}} & \cdots & I_{t_{2,j}} \\ \vdots & \vdots & \ddots & \vdots \\ I_{t_{i,1}} & I_{t_{i,2}} & \cdots & I_{t_{i,j}} \end{bmatrix} \quad (2)$$

where $I_{b_{i,j}}$ represents the induced velocity influence coefficient of the bound vortex segment created by j^{th} blade section on i^{th} blade control point, and $I_{t_{i,j}}$ represents the induced velocity influence coefficient of the two trailed vortices created by j^{th} blade section on i^{th} blade control point, as shown in Fig. 3. The trailed vortices are assumed to be of infinite length. Each blade section generates two trailed vortices, which extend from the segmentation points of the bound vortex. Each trailed vortex shares its geometry with one of the trailed vortices generated by adjacent blade sections. The two trailed vortices produced by the same blade section have opposite vorticity orientations.

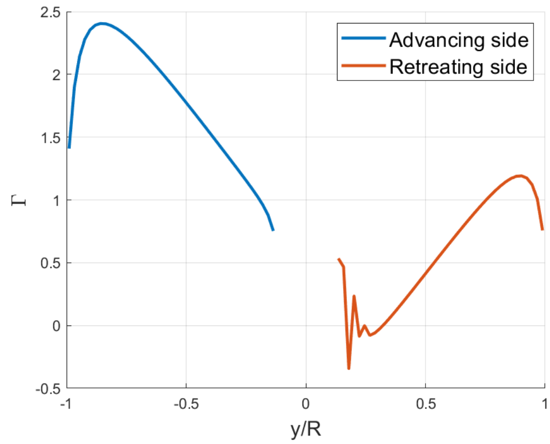

(a) Bound vortex strength variation for the original near-wake model

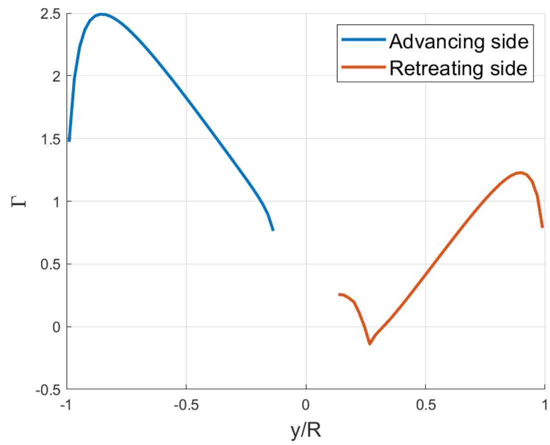

(b) Bound vortex strength variation for the improved near-wake model

Figure 2. Bound vortex strength variation comparison

During simulation, before accounting for the induced velocity influence from the bound vortex and trailed vortex, a preliminary velocity $\boldsymbol{V}_{pre}$ for every blade control point with the contribution from free-stream velocity and far-wake is calculated.

$$\boldsymbol{V}_{pre} = \boldsymbol{V}_{\infty} + \boldsymbol{V}_{far} = \begin{bmatrix} V_{x,pre_1} & V_{x,pre_2} & \cdots & V_{x,pre_i} \\ V_{y,pre_1} & V_{y,pre_2} & \cdots & V_{y,pre_i} \\ V_{z,pre_1} & V_{z,pre_2} & \cdots & V_{z,pre_i} \end{bmatrix} \quad (3)$$

where i represents the index of the local blade section, $\boldsymbol{V}_{\infty}$ and $\boldsymbol{V}_{far}$ represent the velocity contributions from free-stream and far-wake, respectively, and both of them have the same data structure as $\boldsymbol{V}_{pre}$.

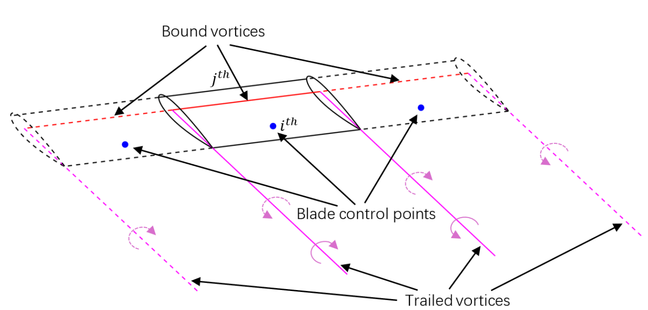

Figure 3. Bound vortices and trailed vortices of the blade

On the retreating blade, at the boundary of the reverse flow region, the local blade control point would experience a rapid change in angle of attack, where the local trailed vortex influence would no longer be accurate. Thus, a diagonal matrix $\boldsymbol{M}_{trail}$ is defined to modify the trailed vortex influence coefficient around the boundary of the reverse flow region.

$$\boldsymbol{M}_{trail} = \begin{bmatrix} M_{t_1} & 0 & \cdots & 0 \\ 0 & M_{t_2} & \cdots & 0 \\ \vdots & \vdots & \ddots & \vdots \\ 0 & 0 & \cdots & M_{t_i} \end{bmatrix} \quad (4)$$

$$M_{t_i} = \cos^2(\alpha_{pre_i}) \begin{cases} \sin\left(0.5\pi \cdot \frac{U_{pre_i}}{4\Omega c}\right), & U_{pre_i} < 4\Omega c \\ 1, & U_{pre_i} \geq 4\Omega c \end{cases} \quad (5)$$

$$\alpha_{pre_i} = \tan^{-1}\left(\frac{V_{z,pre_i}}{V_{y,pre_i}}\right) \quad (6)$$

$$U_{pre_i} = \sqrt{V_{y,pre_i}^2 + V_{z,pre_i}^2} \quad (7)$$

where i represents the index of the local blade section, α_{pre_i} represents the preliminary angle of attack of the local blade control point, U_{pre_i} represents the local velocity magnitude, Ω represents the rotor speed, and c represents the blade chord length.

In addition, within the reverse flow region, since the airflow is moving from the trailing edge to the leading edge, both the local bound vortex and the near wake influence coefficient have to be reversed.

The bound vortex strength to blade control point induced velocity influence coefficient matrix $\boldsymbol{I}_{y,\Gamma_b}$ and $\boldsymbol{I}_{z,\Gamma_b}$ in the y-axis and z-axis respectively is calculated as below.

$$\boldsymbol{I}_{y,\Gamma_b} = \boldsymbol{I}_{trail}\boldsymbol{M}_{trail} \begin{bmatrix} \sin(\alpha_{pre_1}) & 0 & \cdots & 0 \\ 0 & \sin(\alpha_{pre_2}) & \cdots & 0 \\ \vdots & \vdots & \ddots & \vdots \\ 0 & 0 & \cdots & \sin(\alpha_{pre_i}) \end{bmatrix} \quad (8)$$

$$\boldsymbol{I}_{z,\Gamma_b} = (\boldsymbol{I}_{trail}\boldsymbol{M}_{trail} + \boldsymbol{I}_{bound}) \begin{bmatrix} \cos(\alpha_{pre_1}) & 0 & \cdots & 0 \\ 0 & \cos(\alpha_{pre_2}) & \cdots & 0 \\ \vdots & \vdots & \ddots & \vdots \\ 0 & 0 & \cdots & \cos(\alpha_{pre_i}) \end{bmatrix} \quad (9)$$

Within the iterative process in finding the bound vortex strength, we start by calculating the effective velocity on every blade control point.

$$\boldsymbol{V}_{y,eff} = \begin{bmatrix} V_{y,eff_1} \\ V_{y,eff_2} \\ \vdots \\ V_{y,eff_i} \end{bmatrix} = \begin{bmatrix} V_{y,pre_1} \\ V_{y,pre_2} \\ \vdots \\ V_{y,pre_i} \end{bmatrix} - \boldsymbol{I}_{y,\Gamma_b} \begin{bmatrix} \Gamma_{b_1} \\ \Gamma_{b_2} \\ \vdots \\ \Gamma_{b_i} \end{bmatrix} \tag{10}$$

$$\boldsymbol{V}_{z,eff} = \begin{bmatrix} V_{z,eff_1} \\ V_{z,eff_2} \\ \vdots \\ V_{z,eff_i} \end{bmatrix} = \begin{bmatrix} V_{z,pre_1} \\ V_{z,pre_2} \\ \vdots \\ V_{z,pre_i} \end{bmatrix} - \boldsymbol{I}_{z,\Gamma_b} \begin{bmatrix} \Gamma_{b_1} \\ \Gamma_{b_2} \\ \vdots \\ \Gamma_{b_i} \end{bmatrix} \tag{11}$$

where $\boldsymbol{V}_{y,eff}$ and $\boldsymbol{V}_{z,eff}$ represent the effective velocity at every blade control point in the y-axis and z-axis respectively, Γ_{b_i} represents the bound vortex strength, and i represents the index of the local blade control point.

We then calculate the angle of attack and effective velocity magnitude for every blade control point.

$$\alpha_{eff_i} = \tan^{-1}\left(\frac{V_{z,eff_i}}{V_{y,eff_i}}\right) \tag{12}$$

$$U_{eff_i} = \sqrt{V_{y,eff_i}^2 + V_{z,eff_i}^2} \tag{13}$$

With the effective angle of attack for every blade control point, we can find the lift coefficient using a lookup table and then calculate lift per unit span for every blade section using

$$L' = \frac{1}{2}\rho U_{eff}^2 c C_L \tag{14}$$

where L' represents the lift per unit span, ρ represents air density, and C_L represents the lift coefficient. Recalling the Kutta-Joukowski theorem, lift per unit span can also be calculated by the equation:

$$L' = \rho U_{eff} \Gamma_b \tag{15}$$

By combining equations (14) and (15), the following expression can be obtained:

$$\rho U_{eff} \Gamma_b = \frac{1}{2}\rho U_{eff}^2 c C_L \tag{16}$$

This equation must be expanded to its vector form, storing the information of every blade section, and then solving the equation for the values of Γ_{b_i} through iterations.

$$\rho \begin{bmatrix} U_{eff_1} \\ U_{eff_2} \\ \vdots \\ U_{eff_i} \end{bmatrix} \begin{bmatrix} \Gamma_{b_1} \\ \Gamma_{b_2} \\ \vdots \\ \Gamma_{b_i} \end{bmatrix} = \frac{1}{2}\rho \begin{bmatrix} U_{eff_1}^2 \\ U_{eff_2}^2 \\ \vdots \\ U_{eff_i}^2 \end{bmatrix} c \begin{bmatrix} C_{L_1} \\ C_{L_2} \\ \vdots \\ C_{L_i} \end{bmatrix} \tag{17}$$

Improved far-wake generation method

In the original FVW method, only one far-wake is generated per blade, at the blade tip, and the strength of the far-wake section depends on the maximum bound vortex strength. This approach neglects the variation in the bound vortex strength from the blade root to the maximum bound vortex strength. In normal flight scenarios like hover or low-speed forward flight, this far-wake generation method is sufficient to produce an accurate simulation result, as the velocity experienced by the blade tip is significantly higher than the blade root, making the tip vortex dominant in far-wake contribution. However, during high rotor advance ratio or other extreme flight scenarios, for example, when the rotor reduces its RPM temporarily during high-speed forward flight, causing the advance ratio to become very large, the velocity at the blade root becomes comparable to that at the tip. In such cases, the vortex generated at the root may have a significant influence on the far-wake that cannot be ignored. Furthermore, there may be cases where the blade exhibits multiple local maxima in bound vortex strength, such that the absolute maximum may not occur near the tip. Generating the far-wake at the tip using this maximum value could therefore be inappropriate and may lead to instability in the system. This limits the applicability of the original FVW method to only a narrow range of conditions and prevents it from reaching its full potential. To address these limitations, an improved far-wake generation method has been developed in this paper. Rather than solely depending on the maximum bound vortex strength, the proposed method considers the potential influence of the far-wake to be generated.

We first need to calculate the trailed vortex strength Γ_t from the bound vortex strength Γ_b.

$$\Gamma_t = \begin{bmatrix} \Gamma_{t_1} \\ \Gamma_{t_2} \\ \vdots \\ \Gamma_{t_{j-1}} \\ \Gamma_{t_j} \end{bmatrix} = \begin{bmatrix} \Gamma_{b_1} - 0 \\ \Gamma_{b_2} - \Gamma_{b_1} \\ \vdots \\ \Gamma_{b_i} - \Gamma_{b_{i-1}} \\ 0 - \Gamma_{b_i} \end{bmatrix} \tag{18}$$

Note that the number of trailed vortices is always the number of bound vortices plus one.

We can estimate the potential influence of each trailing vortex with the equation below.

$$E_t = \begin{bmatrix} E_{t_1} \\ E_{t_2} \\ \vdots \\ E_{t_j} \end{bmatrix} = \begin{bmatrix} \Gamma_{t_1} U_{t_1} \\ \Gamma_{t_2} U_{t_2} \\ \vdots \\ \Gamma_{t_j} U_{t_j} \end{bmatrix} dt \tag{19}$$

where E_t represents the potential influence of the trailed vortices, U_t represents the velocity magnitude at each trailed vortex creation point, and dt represents the time interval to when the previous far-wake node is created.

In this improved far-wake generation method, it is assumed that adjacent trailed vortices with the same vorticity orientation will combine into a single vortex, as demonstrated in Fig.

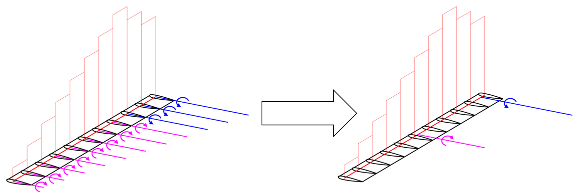

(a) Hovering blade

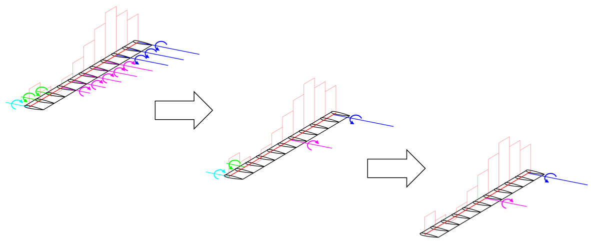

(b) Retreating side blade

Figure 4. Vortex generation demonstration

4a. The resulting combined vortex will carry the cumulative potential influence of the group of trailed vortices that formed it. In some cases, such as a retreating side blade, shown in Fig. 4b, there may be more than two groups of trailed vortices. In such instances, only the two groups of trailed vortices with the highest potential influence are used to generate the vortex, while the remaining groups are discarded. This is because the two dominant groups typically contribute the most to the far wake, and the others have minimal influence and can therefore be ignored to improve overall computational efficiency.

Since there may be cases where trailed vortices, widely across the blade span, are represented by a single vortex, the position and initial core radius of that vortex must be determined with great care. A weighting value is first calculated for each trailed vortex within the same group.

$$w_{t_i} = \frac{E_{t_i}}{\sum E_{t_i}} \tag{20}$$

The weight values of the trailed vortices w_{t_i} describe the potential influence distribution of the trailed vortices in the same group and will be used for calculating the release point and core radius of the far-wake.

$$x_c = \sum (w_{t_i} x_{t_i}) \tag{21}$$

$$r_c = \sqrt{\sum (w_{t_i} |x_{t_i} - x_c|)} \tag{22}$$

where x_c represents the release point of the vortex, r_c represents the vortex core radius, and x_{t_i} represents the position of the individual trailed vortex.

It is also important that the far-wake nodes created in the current time step are connected to the correct nodes created in the previous time step. For example, the far-wake node created at the blade tip in the current time step has to be connected with the node also at the blade tip in the previous time step. However, in some cases, the groups of trailed vortices used for generating far-wake in the current time step are not the same groups in the previous time step, due to the variation in the spanwise bound vortex strength distribution across different azimuths. This could not be avoided, and discontinuities in the vortices created may be observed.

SIMULATION RESULT

The results obtained using the improved FVW method are validated against existing wind tunnel experimental data from (Ref. 14). The simulation model used for obtaining the results combined the improved FVW method with the rotor dynamics model introduced in the authors' previous work (Ref. 15). Fig. 5a illustrates the wake geometry of a rotor in forward flight simulated with the improved FVW method. In addition to tip vortices,the simulation captures additional vortices generated around the mid-span of the blade, accounting for the variation in the bound vortex strength from the blade root to maximum bound vortex strength. Fig. 5b and 5c show the vertical induced velocity along two separate lateral axes behind the rotor, where we may see that the results from the improved FVW method are overall following closely to the experimental results, indicating the good accuracy of the simulation model. However, it can be seen from Fig. 5c that at the advancing side, between $y/R = -0.5$ and $y/R = -1.0$, the induced velocity is not peaking as much as the experimental results. This may be because of the vortex core assumption used in the FVW method, where within the vortex core radius, the induced velocity becomes lower the closer to the vortex core. This assumption is made to prevent numerical instability problems.

To demonstrate the VRPM feature of the improved FVW method, the simulation is initialised with a stationary two-bladed rotor, and the wind velocity is set to $10 m/s$. After 1 second, a constant torque of $5 Nm$ is applied to the rotor to simulate rotor spool-up. Fig. 6a and Fig. 6b show the variation of RPM and rotor thrust over time, respectively. It can be seen that at 1 second, as soon as the torque is applied, the RPM begins to increase. The rotor thrust also begins to rise, with oscillation appearing in the rotor thrust due to the rotor's exposure to the wind, resulting in an uneven load distribution between the advancing and retreating sides. Fig. 7a and Fig. 7b show the variation of RPM and thrust with respect to azimuth once the rotor reaches unaccelerated rotation. It can be seen that the RPM of the rotor is not a predefined controlled input, but rather a state variable, updated through time-step integration. This enables a more accurate simulation of the aerodynamics-dynamics coupling behaviour of the rotors.

Fig. 8 shows a range of wake geometries created by the rotor running at various advance ratios. It is worth noting that the results are displayed for a broad range of advance ratios to demonstrate the capability of the improved FVW method simulating the rotor from non-rotating to its operating RPM. This capability allows for the simulation of AAMs that have separate lifting rotors and propelling rotors, where the lifting rotors may experience a full stop during cruising flight and ac-

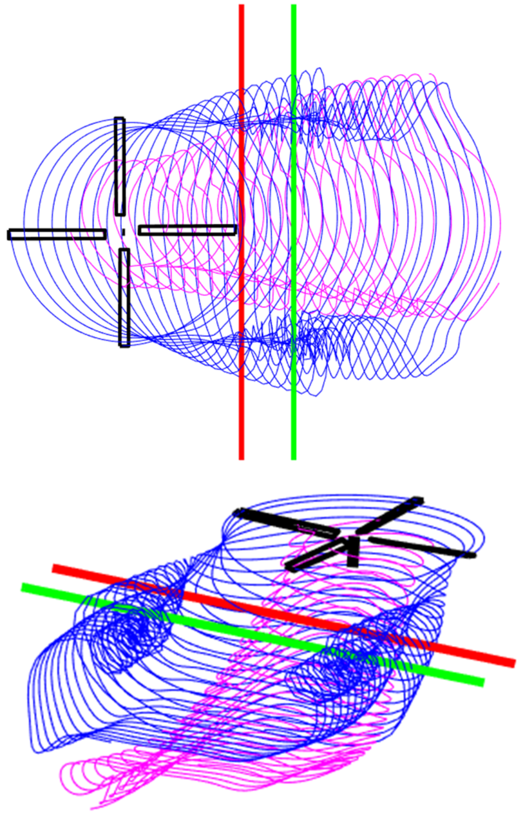

(a) Wake geometry in forward flight ($\mu = 0.075, C_T = 0.00735$)

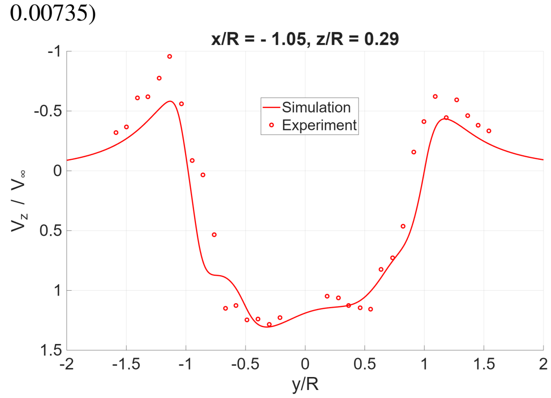

(b) Induced velocity at $x/R = 1.05, z/R = 0.29$

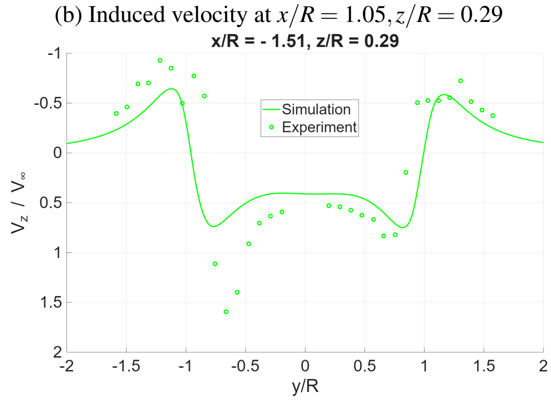

(c) Induced velocity at $x/R = 1.51, z/R = 0.29$

Figure 5. Simulation results of the improved FVW method

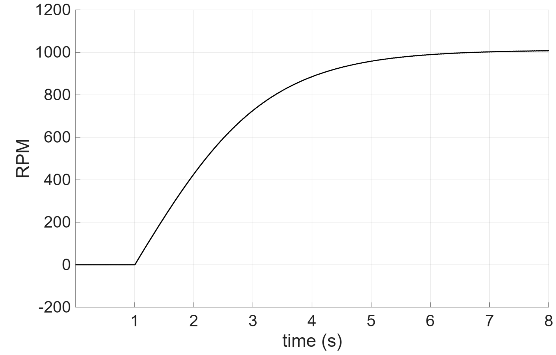

(a) RPM vs time

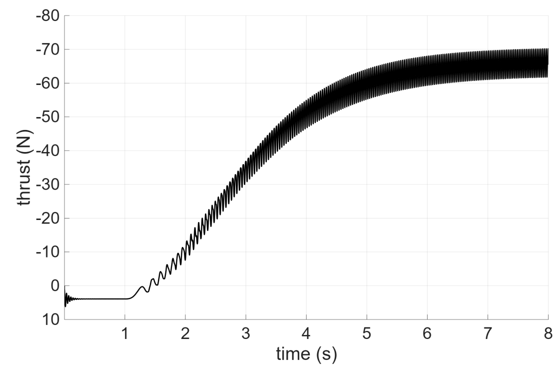

(b) Rotor thrust vs time

Figure 6. Rotor spool-up demonstration

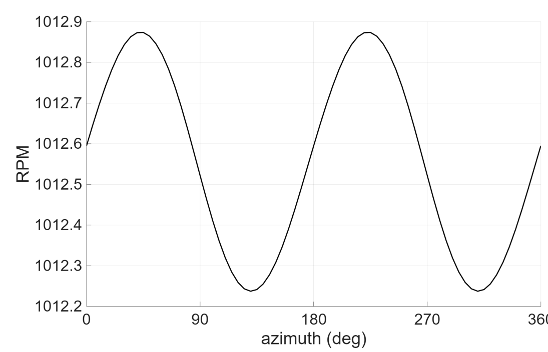

(a) RPM vs azimuth

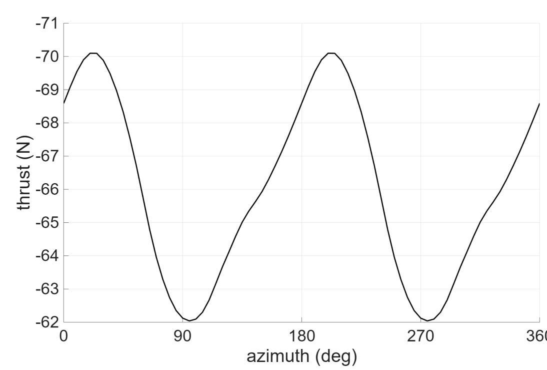

(b) Rotor thrust vs azimuth

Figure 7. Unaccelerated rotation example

celerate back to operating RPM when transforming into hovering flight.

CONCLUSION

With the aim of making it possible to use the FVW method in VRPM conditions, the authors introduced several improvements to the original FVW method, i.e., the planar rigid near-wake reverse flow correction and the improved far-wake generation method. The following points can be concluded from the simulation results obtained with the improved FVW method:

1. The simulation results closely match the experimental results, which indicates the high accuracy of the improved FVW method.

2. Simulation performed with the rotor begin spool-up from non-rotating all the way to operating RPM, highlights the VRPM capability of the improved FVW method.

3. The simulations were able to capture the far-wake generation over a wide-range of advance ratios, even at some extreme advance ratios, displaying the capability of the improved FVW method.

At the time being, the simulation model only supports single-rotor in VRPM conditions, and multi-rotor VRPM simulation is currently under development. Additionally, extensive wind tunnel experiments are planned to be performed in order to validate the simulation model in VRPM conditions.

Authors contact:
Yuxi Chen, PhD candidate, 956110@swansea.ac.uk
Hamed Haddad Khodaparast, Professor, h.haddadkhodaparast@swansea.ac.uk
Alper Celik, Lecturer, alper.celik@swansea.ac.uk
Ye Yuan, Lecturer, ye.yuan@glasgow.ac.uk

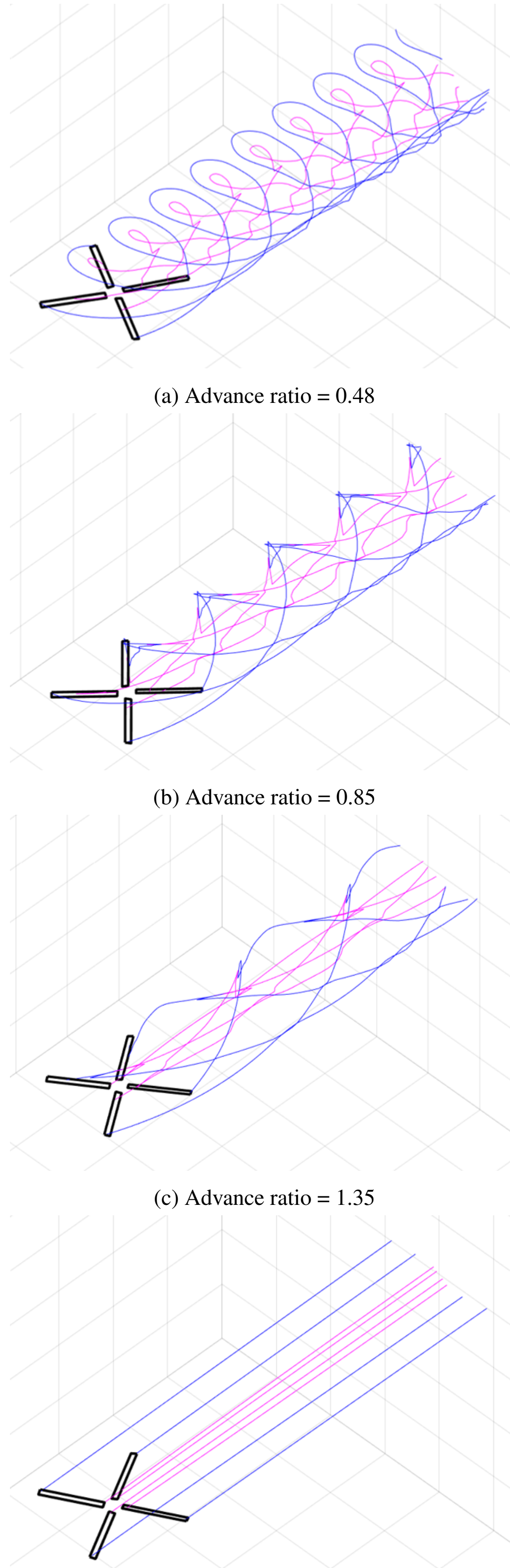

(a) Advance ratio = 0.48

(b) Advance ratio = 0.85

(c) Advance ratio = 1.35

(d) Non-rotating

Figure 8. Advance ratio demonstration

REFERENCES

1. Barakos, G. N., and Filippone, A., "Rotorcraft systems for urban air mobility: A reality check," *The Aeronautical Journal*, Vol. 125, 2021, pp. 3–21. DOI: DOI: 10.1017/aer.2020.52.

2. Al-Rubaye, S., Tsourdos, A., and Namuduri, K., "Advanced Air Mobility Operation and Infrastructure for Sustainable Connected eVTOL Vehicle," *Drones*, Vol. 7, 2023. DOI: 10.3390/drones7050319.

3. Xiang, S., Xie, A., Ye, M., Yan, X., Han, X., Niu, H., Li, Q., and Huang, H., "Autonomous eVTOL: A summary of researches and challenges," *Green Energy and Intelligent Transportation*, Vol. 3, 2024, pp. 100140. DOI: 10.1016/j.geits.2023.100140.

4. Su, J., Huang, H., Zhang, H., Wang, Y., and Wang, F.-Y., "eVTOL Performance Analysis: A Review From Control Perspectives," *IEEE Transactions on Intelligent Vehicles*, 2024.

5. Jimenez-Garcia, A., and Barakos, G. N., "Prediction of helicopter rotor hover performance using high fidelity CFd methods," 35th AIAA Applied Aerodynamics Conference, 2017.

6. ChengLong, Z., YuNong, Y., Wei, L., LinTong, Y., Yang, D., and Rui, Y., "Application of CFD Technology in Rotor Aerodynamic Simulation," 2022 8th International Conference on Mechanical Engineering and Automation Science (ICMEAS), 2022. DOI: 10.1109/ICMEAS57305.2022.00063.

7. Pitt, D. M., and Peters, D. A., "Theoretical prediction of dynamic-inflow derivatives," *Sixth European Rotorcraft and Powered Lift Aircraft Forum*, 1980.

8. Yuan, Y., Chen, R., and Li, P., "Trim investigation for coaxial rigid rotor helicopters using an improved aerodynamic interference model," *Aerospace Science and Technology*, Vol. 85, 2019, pp. 293–304. DOI: https://doi.org/10.1016/j.ast.2018.11.044.

9. Dong, J., Viré, A., Ferreira, C. S., Li, Z., and Bussel, G. V., "A modified free wake vortex ring method for horizontal-axis wind turbines," *Energies*, Vol. 12, 2019, pp. 3900.

10. Padakannaya, R., *The Vortex Lattice Method for the Rotor-Vortex Interaction Problem.*, The Pennsylvania State University, 1973.

11. Bagai, A., *Contributions to the mathematical modeling of rotor flow fields using a pseudo-implicit free-wake analysis*, University of Maryland, College Park, 1995.

12. Saetti, U., *Rotorcraft simulations with coupled flight dynamics, free wake, and acoustics*, The Pennsylvania State University, 2016.

13. Saetti, U., "Real-time simulation of a shipborne rotor via linearized state-space free-vortex wake models," *Journal of Aircraft*, Vol. 61, 2024, pp. 1025–1033.

14. Leishman, J., and Bi, N., "Measurements of a rotor flowfield and the effects on a fuselage in forward flight," *Vertica*, Vol. 14, (3), 1990, pp. 401–415.

15. Chen, Y., Yuan, Y., Khodaparast, H. H., and Celik, A., "Aerodynamics-Dynamics Coupling Investigation for Gimballed Rotor Systems," *10th Asian Australian Rotorcraft Forum*, 2024.